

Visualization and quantification of weathering effects on capillary water uptake of natural building stones by using neutron imaging

Simona Raneri¹ · Germana Barone¹ · Paolo Mazzoleni¹ · Eva Rabot²

Received: 6 June 2016 / Accepted: 12 October 2016 / Published online: 20 October 2016
© Springer-Verlag Berlin Heidelberg 2016

Abstract Building stones are frequently subjected to very intense degradation due to salt crystallization, often responsible for strong modifications of their pore network. These effects have a great influence on the mechanical properties and durability of the materials, and on the penetration of water. Therefore, the quantification and visualization of water absorption into the pore network of degraded stones could provide useful information to better understand the weathering process. In this study, neutron radiography has been used (1) to monitor and visualize in two dimensions the capillary water uptake in a Sicilian calcarenite widely used as building and replace stone (namely Sabucina stone) and (2) to quantify the water content distribution, as a function of time and weathering degree. Additionally, traditional experiments based on gravimetric methods have been performed, following the standard recommendations. Results demonstrated a change in the physical properties of Sabucina stones with the intensification of the degradation process, with severe effects on the capillary imbibition dynamics. The water penetration depth at the end of the experiment was substantially higher in the fresh than in the weathered stones. The water absorption kinetics was faster in the weathered samples, and the amount of water absorbed increased with the number of weathering cycles. Good agreement between classical and neutron imaging data has also been

evidenced. However, neutron radiography has allowed retrieving additional spatial information on the water absorption process, and to better understand how salt weathering affects the petrophysical properties of the studied stone and how it influences then the stone response against water.

1 Introduction

Capillary water uptake is one of the main processes driving water penetration in natural building stones, usually described by the capillary absorption coefficient. Capillary absorption coefficient is determined following, e.g., the UNI 10859:2000 standard recommendation [1] and expressed as the amount of water uptake per square meter as a function of the square root of time. It provides useful information on the material properties when liquids spread over solid surfaces. However, this parameter reflects an overall behavior of the material, without providing detailed information on the dynamic chemical and physical processes that occur when aqueous solutions move and react with the material through its pore system. These aspects are of particular interest in heritage engineering and conservation fields, since water is considered to be the main deterioration agent of buildings and monuments [2]. Indeed, the flow of aqueous solutions and the subsequent chemical and physical interactions with porous materials often lead to degradation due to freeze/thaw cycles, solvent action of water and/or salt crystallization. In this context, the visualization and quantification of water absorption into the pore network of stones could provide additional information on these degradation phenomena.

Over the last few years, the use of innovative, noninvasive, and nondestructive techniques, able to characterize

✉ Paolo Mazzoleni
pmazzol@unict.it

¹ Department of Biological, Geological and Environment Sciences, University of Catania, Corso Italia 57, 95129 Catania, Italy

² Laboratoire Léon Brillouin (CNRS/CEA), CEA Saclay, 91191 Gif-Sur-Yvette, France

both sub-surface and surface features of porous materials, has largely increased, especially in stone conservation studies. Nuclear magnetic resonance applications have been widely used to study the porosity and permeability of rock materials [3, 4]. Among the imaging techniques, neutron and X-ray imaging methods have proved to be valuable procedures to investigate the internal structure of archaeological, geological, and industrial materials [5, 6]. Image analyses are not limited to simple 2-D or 3-D representations of the studied objects, as a large amount of quantitative indicators can be extracted. Neutron imaging has proved to be particularly efficient for studying hydrogen-rich fluid dynamics in non-hydrogenous porous media. Indeed, the significant difference in the attenuation coefficients of water, solid, and air results in highly contrasted transmission images, so that detailed information on the arrangement of solid particles, liquid phase, and voids can be achieved. In addition, neutron imaging allows performing dynamic measurements to monitor water uptake as a function of time, and therefore to explore the complex processes involved in fluid movement through porous materials. Neutrons have successfully been used for studying porous stones, and several examples are available in the literature [7–13]. In cultural heritage and industrial sciences, neutrons have been used to visualize water movements in building stones, sometimes in combination with X-ray computed tomography [14], and to investigate weathering effects or efficiency of water repellents [15–17] and consolidant products [18, 19].

In this study, we used neutron radiography to highlight the influence of changes in the pore network due to salt crystallization on the capillary water uptake of a Sicilian calcarenite used as building and replace stone (Sabucina stone). We performed dynamic neutron imaging experiments involving capillary water uptake into artificially degraded samples. Neutron radiography allowed quantifying the movement of the capillary wetting front by deriving the water content and sorptivity. Classical gravimetric tests were also performed to compare neutron imaging results with standard tests.

2 Experimental

2.1 Stone samples and weathering

Sabucina stone is a coarse-grained and yellowish calcarenite used as a building and replace stone in Sicilian monuments [20]. According to the Folk classification [21], it exhibits a microscopic texture varying between grain stone and pack stone, with allochems mainly formed by small fragments of mollusca (200 μm to 1.5 mm in dimension), and orthochems due to sparitic calcite and

micrite, irregularly distributed. A silicoclastic phase (2–3 %) is composed of sub-rounded grains of quartz (100 μm mean diameter). The mineral matrix is primarily composed of calcium carbonate (c.a. 90 %), with quartz (c.a. 5 %), and dolomite (c.a. 5 %). Sabucina stone is classified as biosparite according to the Dunham nomenclature [22]. Porosity, mainly interparticle, moldic, and vuggy [23], reaches approximately 27 %, with a total pore volume of 0.14 $\text{cm}^3 \text{g}^{-1}$. Referring to the pore size distribution, Sabucina stone exhibits a modal pore radius of about 8.5 μm . Capillary and total water absorption coefficients are 0.02 g cm^{-2} and 11.07 %, respectively. Further details on the petrography, mineralogy, chemical composition, petrophysics, and porosimetry of Sabucina stones are provided in Barone et al. [24].

For this study, weathered Sabucina stone samples have been obtained according to the UNI EN 12370:2001 standard [25] on the resistance of natural stones to crystallization damages. Briefly, parallelepiped samples of $2 \times 2 \times 4 \text{ cm}^3$ have been subjected to immersion-drying cycles, by using a solution of sodium sulfate (14 % v/v). Water evaporation has led to the crystallization and accumulation of thenardite (Na_2SO_4) or mirabilite ($\text{Na}_2\text{SO}_4 \cdot 10\text{H}_2\text{O}$), at low and high relative humidity, respectively. Unweathered samples and artificially weathered samples subjected to 4, 8, 12, and 15 cycles of immersion-drying have been selected for the neutron imaging experiments and gravimetric tests (3 replicates). Indeed, from a previous study [24], we know that the degradation mechanism in Sabucina stones consists first in a gain of mass, approximately up to the 6th cycle, followed by a continuous loss of mass. The dimensions of each sample have been thoroughly measured to report results on a surface basis in the following.

2.2 Neutron imaging and image processing

Neutron imaging has been performed using the IMAGINE station at the Laboratoire Léon Brillouin, CEA Saclay, France. IMAGINE uses cold neutrons with wavelengths from 3 to 20 \AA . The detector was placed at $L = 4 \text{ m}$ from the aperture, and the aperture diameter was $D = 10 \text{ mm}$, giving $L/D = 400$. The neutron flux was $2.10^7 \text{ neutrons s}^{-1} \text{ cm}^{-2}$. A sCMOS camera (Andor) coupled with a lithium scintillator of 100 μm thickness was used for data acquisition. In this configuration, the spatial resolution was 250 μm . Radiographs were acquired every 40 s, with an exposure time of 40 s.

Ten dark field images (i.e., neutron beam closed, without any sample) and open beam images (i.e., neutron beam open, without any sample) have been first acquired. Samples were placed in an aluminum container, between the source and the detector. Then, a reference radiograph of the

initial dry sample has been taken for the subsequent quantitative evaluation. The aluminum container has been manually filled with 3 mm of water, to wet the sample from the bottom by capillary rise. Immediately after the water addition, radiographs have been acquired at regular time intervals until saturation, to monitor the water absorption as a function of time. The length of the experiment was approximately 20 min.

Radiographs have been processed by using the ImageJ software [26]. First of all, a possible offset of the camera has been corrected by subtracting the mean dark field image to every image. This has also been done to the mean open beam image. Then, every image has been normalized, by dividing them by the corrected mean open beam image, to remove the effect of the non-homogeneity in the neutron beam. Pixel values in the normalized radiographs thus ranged between 0 and 1. Additionally, a spot filter has been applied to remove pixels due to noise.

The quantification of the water content distribution inside the stones has been obtained according to Kim et al. [27]. By normalizing a wet image (I_{wet}) by the dry reference image (I_{dry}) of the same stone sample, the 2-D distribution of the water thickness (d_w) at each pixel position (x, y) is obtained from Eq. (1):

$$d_w(x, y) = - \frac{\ln \left[\frac{I_{wet}(x, y)}{I_{dry}(x, y)} \right]}{\Sigma_w} \quad (1)$$

with $I_{dry}(x, y) = I_0(x, y) \cdot e^{-\Sigma_s d_s}$; $I_{wet}(x, y) = I_0(x, y) \cdot e^{-(\Sigma_w d_w + \Sigma_s d_s)}$; Σ_w and Σ_s , the attenuation coefficients of water and dry stone, respectively. By dividing the water thickness by the measured thickness of the sample (d_c), the water content (WC%) of each pixel can simply be calculated from Eq. (2):

$$WC(x, y) = \frac{d_w(x, y)}{d_c(x, y)} \cdot 100 \quad (2)$$

Moreover, in order to describe the capillary water uptake process, the sorptivity parameter (B) has been determined experimentally from the radiographs, by recording the position of the wetting front with time. In detail, B has been determined according to Philip [28]:

$$B = \frac{x_{wf}}{t^{0.5}} \quad (3)$$

where x_{wf} is the wetting front position, equivalent to the cumulative infiltration per unit area, and t is the time.

2.3 Gravimetric tests

In order to compare the results obtained by using a non-destructive imaging technique and classical gravimetric methods, absorption experiments have also been performed

in the laboratory, following standard recommendations. In detail, the capillary absorption coefficient has been determined following the UNI 10859:2000 standard recommendation [1] on unweathered and weathered samples. The amount of water absorbed by capillarity (Q_i) has been measured at regular time steps i and reported as a function of the square root of time ($t^{0.5}$). The absorption coefficient AC ($\text{g cm}^{-2} \text{t}^{-0.5}$) has been estimated as the slope of the curve $Q_i = f(t^{0.5})$ for $0 < t < 30$ min, when the function is approximately linear (according to the model of capillary absorption). Additionally, the free and forced water absorptions have been estimated by performing water absorption tests, at atmospheric pressure and under vacuum, respectively. The interconnection between pores (A_x) [29] and saturation coefficient (S) [30] has been calculated as follows:

$$A_x = \frac{A_f - A_b}{A_f} \cdot 100 \quad (4)$$

$$S = \frac{M_{48h} - M_0}{M_S - M_0} \cdot 100 \quad (5)$$

with $A_b = \frac{M_L - M_0}{M_0} \cdot 100$, the free water absorption at atmospheric pressure; $A_f = \frac{M_S - M_0}{M_0} \cdot 100$, the forced water absorption under vacuum; M_0 , the mass of the dry sample (g); M_L , the mass of the sample saturated with water at atmospheric pressure, until constant mass is reached (g); M_{48h} , the mass of the sample after 48 h immersion in water at atmospheric pressure (g); M_S , the mass of the sample saturated under vacuum (g).

3 Results

3.1 Weathering effect observed with neutron imaging

The capillary water uptake monitored with neutron radiography is presented in Fig. 1. In detail, radiographs acquired 5, 10, 15, and 20 min after the addition of water for an unweathered sample and for samples representative of different degradation degrees are shown, as an example. The dry image is formed from the attenuation of neutrons through the solid particles and air, while the wet images are the result of the sum of the attenuations associated with water, solid particles, and air. Therefore, by normalizing a wet image with a dry reference image of a given stone sample, the 2-D distribution of water can be visualized and the position of the wetting front can be determined from the relative water content profiles. The inspection of the raw neutron radiographs clearly suggests that, in the studied samples, the wetting front is not planar. For this reason, the evaluation of its position has been performed by selecting a

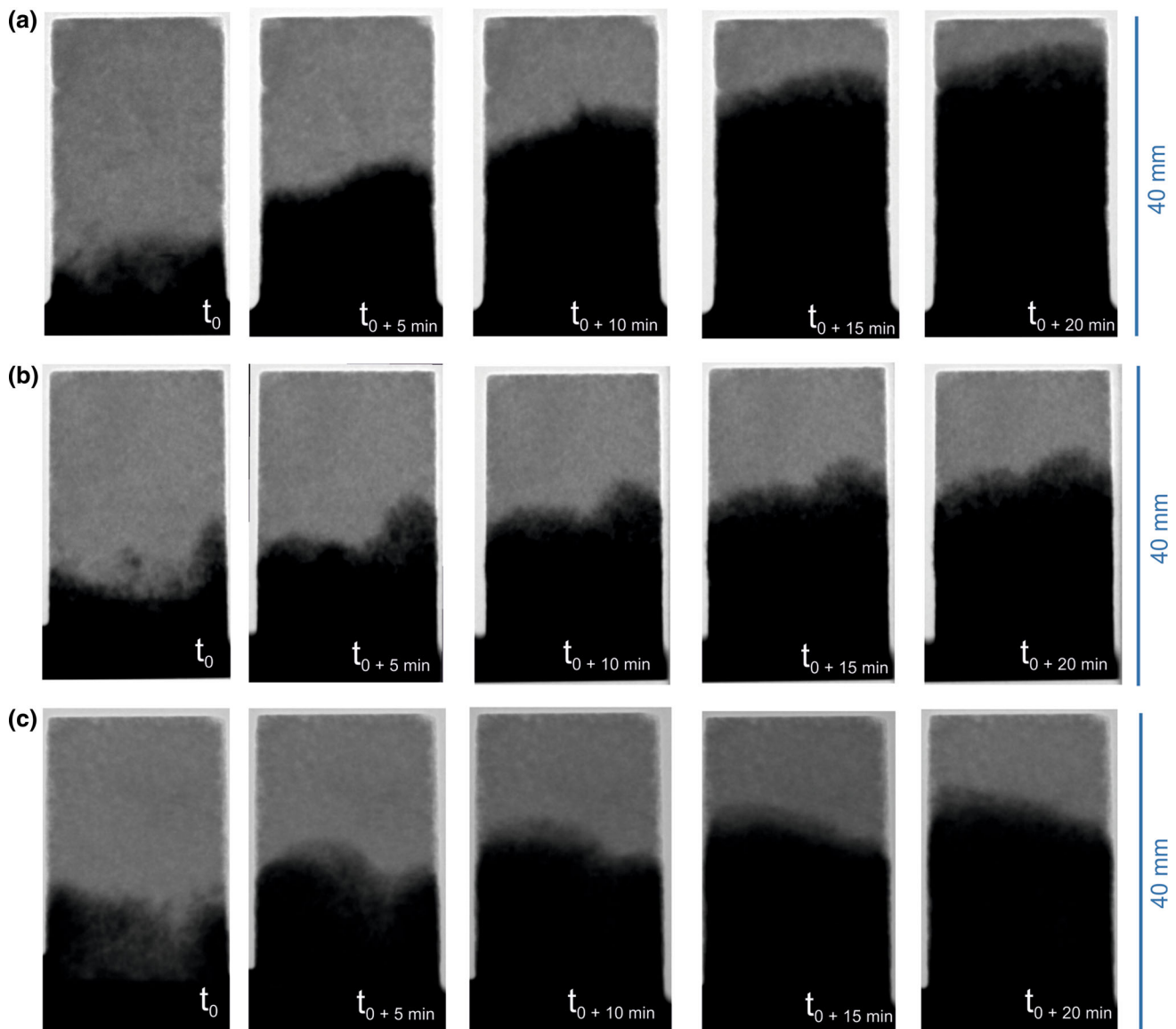


Fig. 1 Examples of normalized neutron radiographs at selected time steps during capillary water uptake by Sabucina stones: **a** unweathered sample and samples subjected to **b** 8 and **c** 15 artificial weathering

cycles. *Light gray areas* indicate dry conditions, while *dark gray areas* indicate saturation conditions

vertical column of pixels centered in the samples. In this way, lateral and edge effects have been eliminated and the one-dimensional capillary rise of water has been quantified. In Fig. 2, the profiles of intensity values at selected time steps obtained from the transmission images are reported. From them, the wetting front position can be determined as the inflection point of the profile, indicating the transition between dark gray values (saturation) and lighter ones (dry conditions). The resulting wetting front positions have been related to time using Eq. (3), and the results are reported in Fig. 3, where the linearity of the relationship between the wetting front position and the square root of time is clearly illustrated. The sorptivity values have been determined by

using linear regression (Table 1). The associated coefficients of determination (R^2), largely >0.95 , indicate good fits with minimal dispersion around the regression lines for this protocol.

In order to quantify the water distribution in the stone samples and to better understand the water uptake process, the thickness of water crossed by the neutron beam as a function of time has been estimated. In Fig. 4, examples of contour plots of the water content distribution (WC%) estimated from the neutron radiographs at 5, 10, 15, and 20 min after the water addition are shown. It is worth noting that the contact time labeled as t_0 has to be considered as a reference start value for the evaluation of the

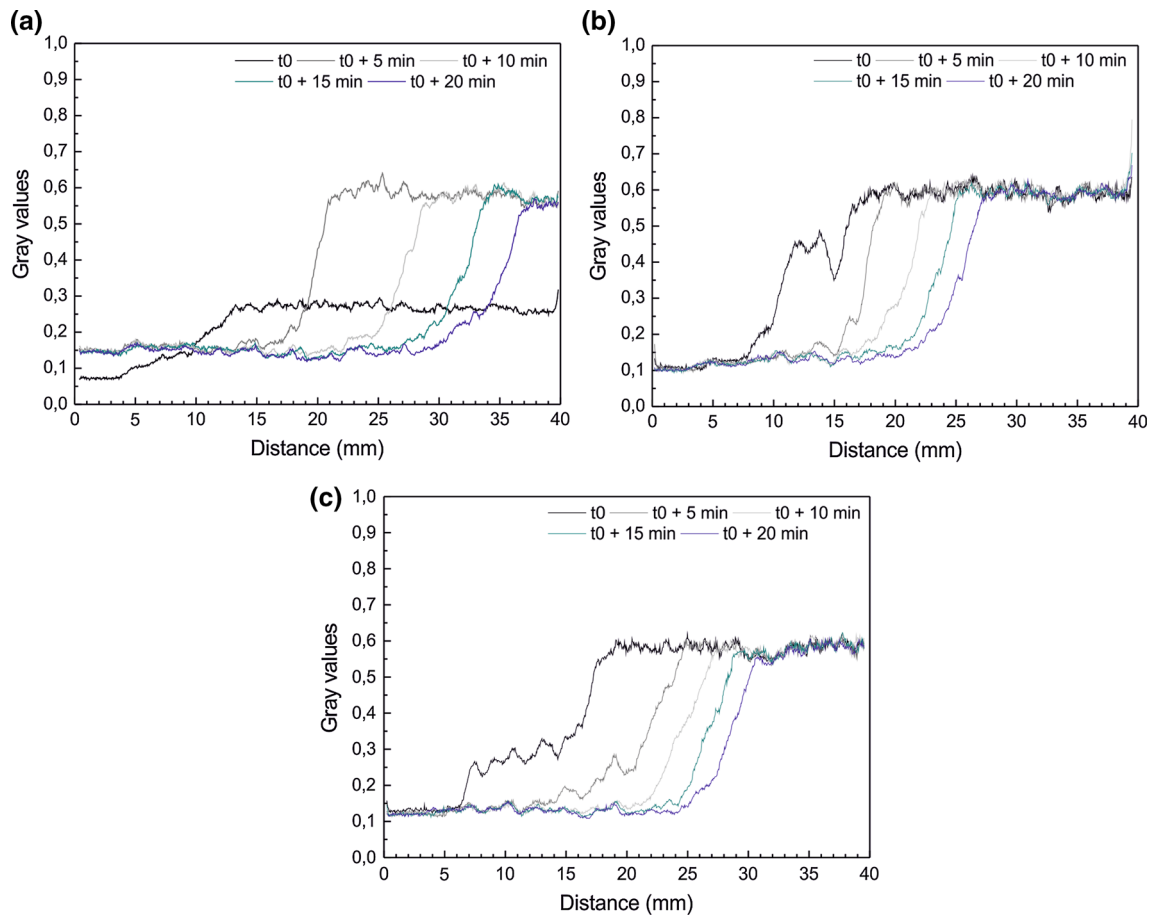


Fig. 2 Profiles of intensity values at selected time steps during capillary water uptake by Sabucina stones. Profiles of **a** unweathered sample and samples subjected to **b** 8 and **c** 15 artificial weathering cycles. The 0 reference distance is the bottom of the sample

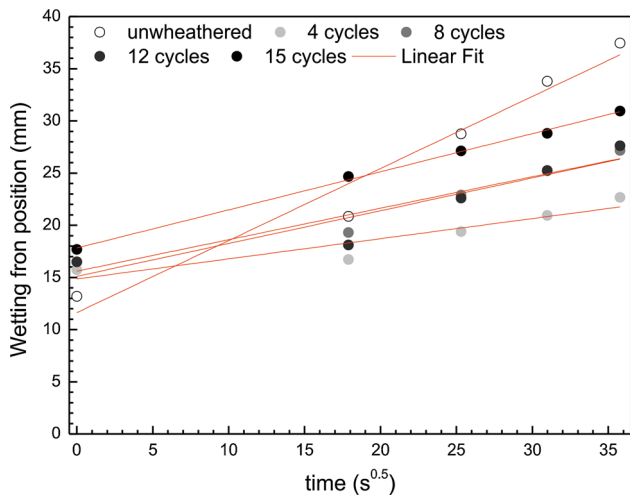


Fig. 3 Wetting front position as a function of the square root of time, for increasing numbers of artificial weathering cycles. The slope of the linear regression indicates the sorptivity; as examples: unweathered sample ($y = 0.69x + 11.62$, $R^2 = 0.96$), 8 cycles ($y = 0.30x + 15.59$, $R^2 = 0.93$), 15 cycles ($y = 0.36x + 17.81$, $R^2 = 0.99$)

Table 1 Sorptivity of unweathered and weathered Sabucina stone samples subjected to increasing numbers of artificial weathering cycles, estimated from the neutron radiographs and Eq. (3)

Artificial weathering steps	Sorptivity ($\text{mm s}^{-0.5}$)
None	0.69
4 cycles	0.19
8 cycles	0.30
12 cycles	0.31
15 cycles	0.36

whole sequence, as it effectively represents the first wet acquisition available after the manual addition of water and the opening of the neutron beam in safe conditions. Contours describing the quantitative distribution of water inside the stone volumes clearly show that the penetration depth of water at the end of the experiment was substantially higher in the unweathered sample than in the weathered ones. Higher amount of water was absorbed by

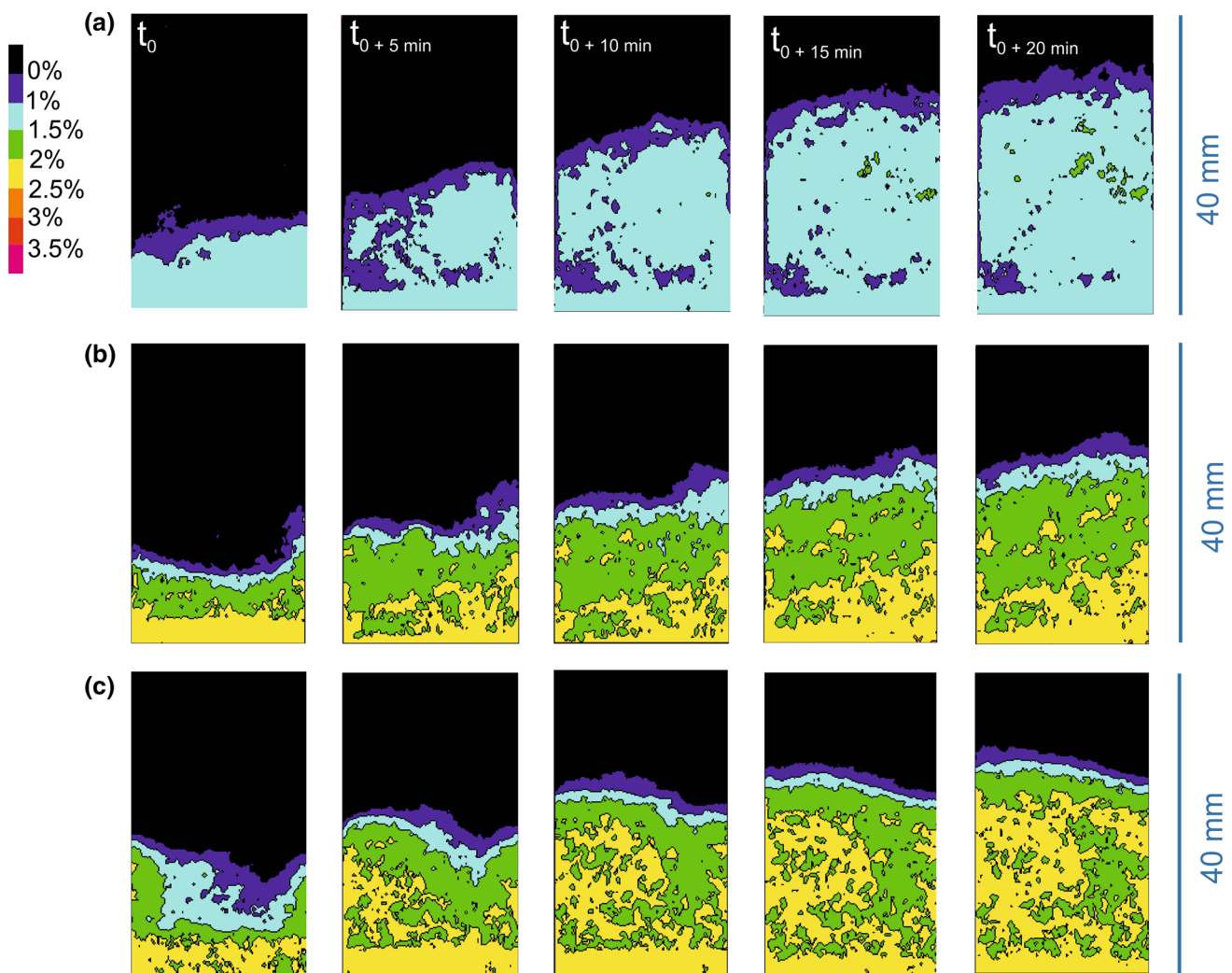


Fig. 4 Contour maps of the water content estimated from the neutron radiographs at selected time steps during capillary water uptake by Sabucina stones: **a** unweathered sample and samples subjected to **b** 8 and **c** 15 artificial weathering cycles

the weathered samples as compared to the unweathered sample. Figure 4 also highlights the heterogeneity of the pore space of the artificially weathered samples. Additionally, the more intense action of the degradation process close to the surface is evidenced by the fast advancement of the wetting front and the high WC% at the edges of the weathered stone samples as compared to the inner part in the early time steps of the experiment.

3.2 Capillary absorption coefficient, saturation, and interconnection parameters from gravimetric tests

In Table 2, the results obtained for the capillary absorption test according to the UNI 10859:2000 standard recommendation [1] are reported, while the amount of water absorbed per area as a function of time during the first 30 min (equivalent to $42 \text{ s}^{0.5}$) of water

absorption by capillarity is shown in Fig. 5. The evolution of the capillary absorption within this time interval is highly informative, since it is related to the determination of the absorption coefficient AC. As can be inferred from the inspection of the curves, for both unweathered and weathered samples, the function is fairly linear, with a slope increasing along with the weathering process. This indicates a relation between the water absorbed per unit cross section and the sample degradation degree, with an increase of the amount of absorbed water in the first 30 min, from about 0.61 g cm^{-2} (70 %) to 0.68 g cm^{-2} (82 %), for the 4-cycle and the 15-cycle treatments, respectively. Additionally, changes in absorption properties are evidenced by an increase of the absorption coefficient values with the number of weathering cycles (Table 2). Substantial modifications are also visible in terms of saturation coefficient S : an increase of the saturation

Table 2 Report of the UNI 10859 standard recommendation test

\sqrt{t} ($s^{0.5}$)	Water absorption per area ($g\ cm^{-2}$)					Water absorption per area (% total water absorbed)				
	Unweathered	4 cycles	8 cycles	12 cycles	15 cycles	Unweathered	4 cycles	8 cycles	12 cycles	15 cycles
0	0	0	0	0	0	0.00	0.00	0.00	0.00	0.00
13	0.28 ± 0.03	0.32 ± 0.02	0.36 ± 0.06	0.38 ± 0.07	0.43 ± 0	30.91	36.60	42.35	44.39	52.41
17	0.39 ± 0.05	0.40 ± 0.04	0.43 ± 0.08	0.46 ± 0.08	0.49 ± 0.01	42.56	46.09	49.56	52.98	60.10
24	0.45 ± 0.06	0.45 ± 0.06	0.47 ± 0.09	0.50 ± 0.09	0.54 ± 0.01	49.56	51.84	54.86	58.65	65.62
35	0.56 ± 0.09	0.54 ± 0.09	0.55 ± 0.1	0.60 ± 0.1	0.63 ± 0.03	61.88	63.20	64.33	70.10	76.42
42	0.64 ± 0	0.61 ± 0.01	0.61 ± 0.01	0.66 ± 0.01	0.68 ± 0.04	70.96	71.38	71.36	77.18	82.84
60	0.77 ± 0.05	0.72 ± 0.09	0.71 ± 0.05	0.74 ± 0.01	0.73 ± 0.03	84.43	83.54	82.36	85.62	88.76
85	0.80 ± 0.04	0.77 ± 0.06	0.77 ± 0.05	0.76 ± 0.07	0.73 ± 0.03	88.21	89.17	88.95	88.52	89.02
147	0.80 ± 0.04	0.78 ± 0.06	0.78 ± 0.05	0.76 ± 0.03	0.73 ± 0.03	88.42	90.39	90.45	88.93	89.17
170	0.81 ± 0.04	0.78 ± 0.06	0.79 ± 0.05	0.77 ± 0.03	0.74 ± 0.03	89.08	91.09	91.96	90.08	90.70
294	0.83 ± 0.04	0.80 ± 0.06	0.81 ± 0.05	0.80 ± 0.04	0.76 ± 0.03	91.73	93.33	93.85	92.73	92.92
416	0.85 ± 0.04	0.82 ± 0.06	0.82 ± 0.05	0.81 ± 0.04	0.77 ± 0.03	93.87	95.00	95.43	94.36	94.43
509	0.87 ± 0.04	0.83 ± 0.06	0.83 ± 0.05	0.82 ± 0.04	0.78 ± 0.03	95.53	95.87	96.23	95.40	95.71
588	0.88 ± 0.04	0.83 ± 0.06	0.84 ± 0.05	0.83 ± 0.04	0.79 ± 0.03	96.68	96.92	97.11	96.40	96.53
778	0.89 ± 0.04	0.85 ± 0.06	0.85 ± 0.05	0.84 ± 0.04	0.80 ± 0.03	98.57	98.45	98.49	98.03	98.14
831	0.90 ± 0.04	0.85 ± 0.06	0.85 ± 0.05	0.85 ± 0.04	0.81 ± 0.03	99.22	99.08	99.13	98.86	98.93
882	0.91 ± 0.04	0.86 ± 0	0.86 ± 0.05	0.86 ± 0.04	0.81 ± 0.03	99.95	99.71	99.51	99.56	99.18
930	0.91 ± 0.04	0.86 ± 0	0.86 ± 0.05	0.86 ± 0.04	0.81 ± 0.03	100.00	99.88	99.98	99.85	99.44
975		0.86 ± 0	0.86 ± 0.05	0.86 ± 0.04	0.82 ± 0.03		100.00	100.00	100.00	100.00
AC ($g\ cm^{-2}\ t^{-0.5}$)	0.03 ± 0.01	0.04 ± 0.01	0.04 ± 0.01	0.05 ± 0.01	0.05 ± 0.01					

The water absorbed by capillarity (in terms of $g\ cm^{-2}$ and percentage of total water absorbed as a function of the square root of time $t^{0.5}$) is reported for samples subjected to increasing numbers of artificial weathering cycles. Average values assessed on three specimens representative of each weathering step and standard deviations are reported. The absorption coefficient AC at different degradation steps is finally proposed. The values at the first 30 min (equivalent to $42\ s^{0.5}$) are highlighted in bold.

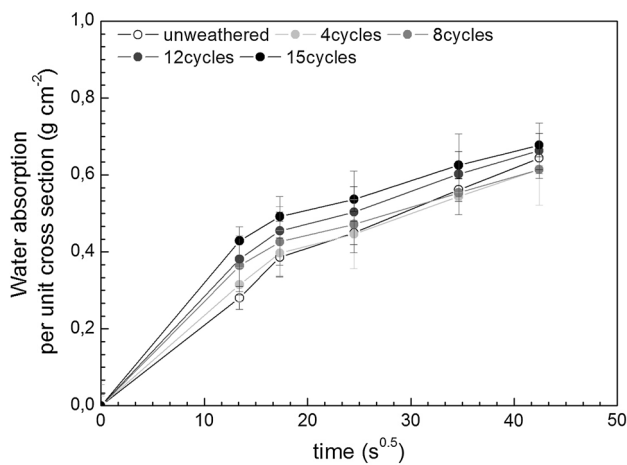


Fig. 5 Water absorbed as a function of time during the first 30 min of water absorption by capillarity, for samples subjected to increasing numbers of weathering cycles, measured from gravimetric tests. Error bars represent standard deviation

coefficient can be observed with the number of weathering cycles, with no substantial changes in the interconnection between pores (Table 3).

4 Discussion

As expected, for all samples, the waterfront moved proportionally to the square root of time. However, clear differences in the capillary properties were evidenced between unweathered and weathered samples, as well as among samples subjected to increasing weathering cycles. Going into details, the distance traveled by the wetting front at the end of the experiment appeared higher in the unweathered sample as compared to the weathered ones, even if an increase of these values can be observed along the weathering process. Referring this time to the kinetics, capillary imbibition was faster in the unweathered sample (sorptivity $\sim 0.7\ mm\ s^{-0.5}$) than in the weathered ones, in which sorptivity values ranged between ~ 0.2 and $0.4\ mm\ s^{-0.5}$. Such a behavior can be hypothetically explained considering: (1) the influence of petrography and pore structure on capillary processes in natural building stones [30] and (2) the degradation mechanism in the studied stone. In this sense, the results obtained from the images can be better understood in the light of gravimetric

Table 3 Free water absorption at atmospheric pressure (A_b), forced water absorption under vacuum (A_f), interconnection between pores (A_x), and saturation coefficient (S) obtained for unweathered and weathered Sabucina stones subjected to increasing numbers of artificial weathering cycles

Artificial weathering steps	M_0 (g)	M_L (g)	M_S (g)	M_{48h} (g)	A_b (%)	A_f (%)	A_x (%)	S (%)
None	119.08 ± 5.94	134.46 ± 5.37	138.90 ± 5.54	133.31 ± 5.45	12.91 ± 1.18	16.64 ± 1.19	22.42 ± 1.8	71.81 ± 1.38
4 cycles	115.90 ± 1.80	130.54 ± 2.47	134.64 ± 2.48	129.54 ± 2.42	12.63 ± 0.9	16.16 ± 0.89	21.87 ± 1.23	72.79 ± 1.16
8 cycles	116.88 ± 4.64	131.73 ± 3.91	135.83 ± 4.07	130.84 ± 3.93	12.71 ± 1.23	16.21 ± 1.71	21.62 ± 0.75	73.65 ± 0.98
12 cycles	112.87 ± 5.07	127.62 ± 4.36	131.82 ± 3.98	126.73 ± 4.45	13.07 ± 1.21	16.79 ± 1.71	22.17 ± 0.75	73.17 ± 0.98
15 cycles	108.28 ± 5.08	122.19 ± 5.44	125.98 ± 5.68	122.02 ± 5.82	12.85 ± 0.56	16.35 ± 0.84	21.43 ± 1.02	77.65 ± 2.92

Average parameters assessed on three specimens representative of each weathering step and standard deviations are reported. M_0 = mass of the dry sample; M_L = mass of the sample saturated at atmospheric pressure; M_S = mass of the sample saturated under vacuum; M_{48h} = mass of the sample after 48 h immersion in water at atmospheric pressure

tests and previous studies aiming to analyze the effects of salt weathering on the pore structure of coarse-grained calcarenites [24, 31].

Taking advantage of previous experimental researches based on the application of X-ray tomography [31] and porosimetry analyses [24], we know that the weathering of Sabucina stones leads to an initial decrease of the total and open porosity till the 6th crystallization cycle (i.e., total porosity decreases from ~11 to ~9 %). Changes occurring in this first stage of salt weathering have to be related to the filling of pore throats, of about 50–100 μm in diameter, by salts. Then, when the weathering proceeds, total and open porosity increases (i.e., total porosity increases from ~9 to ~15 %) and pores are enlarged (i.e., increase in the volume of pores >350 μm in diameter). Therefore, the differences in the wetting front positions observed in the present study with neutron radiography can be explained according to the Jurin's law (i.e., the height of a capillary column of liquid is inversely proportional to the diameter of the tube): the water penetration was deeper in unweathered conditions than in the latest steps of weathering because of thinner pores in the unweathered sample.

The weathering process also influenced the kinetics, since the succession of throats and pores with their respective radii strongly controls the water capillary absorption in natural stones [30]. In detail, the thinner the throats are, the slower the kinetics proceeds. By analyzing the neutron radiographs, we could monitor a drastic reduction of sorptivity in the weathered samples. It can be explained by the filling of the pore entries and the consequent modification of the pore network morphology, so that the pore diameters, the volume of open porosity, and thus the pore connectivity were probably reduced on the first steps of weathering. On the contrary, when pore throats have been enlarged, especially from the 8th cycle, the connectivity could have increased and the weathered stones became able to absorb water faster as compared to the

unweathered ones. Weathered stones were also able to absorb much more water, as seen in the contour plots derived from the radiographs (Fig. 4), in which WC% reached 2.5 % within the first minutes of contact with water.

The ability of weathered stones to absorb greater volumes of water has also been evidenced by the increase of the capillary and saturation coefficients with the intensification of the degradation process, as estimated by classical gravimetric methods. Nevertheless, even if data previously acquired by using X-ray tomography and porosimetry, together with gravimetric tests, certainly help understanding the different hydric behaviors of unweathered and weathered stones, the critical inspection of the radiographs clearly suggests that the calculated parameters were insufficient to describe the heterogeneous water movement inside the stones. Neutron radiography allowed retrieving additional spatial information on the water absorption process, such as the depth of water penetration and the identification of non-horizontal waterfronts. Moreover, in the weathered samples, the water distribution was especially heterogeneous, with the establishment of areas of higher WC% than the surrounding. These observations on the vertical and lateral water distributions have, of course, implications for the depth and intensity of the degradation process during subsequent drying and water absorption cycles.

5 Conclusion

In this study, we used neutron radiography to characterize the effect of weathering on the hydric behavior of a calcarenite used as a building and replace stone in Sicilian monuments, through its capillary water uptake. Neutron imaging allowed monitoring the evolution of the wetting front position and water content as a function of time.

Weathering appeared to actually affect the behavior of this stone against water. The water penetration depth at the end of the experiment was substantially higher in the unweathered than in the weathered stones. However, the dynamics of water absorption was faster in the weathered samples, as observed by the sorptivity values derived from the image analysis, and the amount of water absorbed increased with the number of weathering cycles. By interpreting these observations according to the laws driving water movement in porous media, together with previous published data using X-ray computed tomography, mercury porosimetry, and gravimetric tests, we could formulate a hypothesis on the weathering process in the studied stones. In the early stages of weathering, the pore network was greatly modified by the crystallization of salts on pore throats, reducing total porosity, mean pore diameter, and connectivity of the pore network. Penetration depth and sorptivity were thus drastically reduced as compared to fresh samples. Then, the weathering process tended to increase the porosity and to enlarge pores, allowing larger amount of water to be retained in weathered samples.

The use of neutron imaging allowed us to better understand how salt weathering affects the petrophysical properties of the studied stone and how it influences then the stone response against water, highlighting the role of the pore geometry in the capillary absorption. The good agreement found between data derived from neutron radiography and some other published data suggests that gravimetric analyses and mercury porosimetry still provide useful and reliable indicators (i.e., porosity, saturation, interconnection between pores). However, water being easily identified, even at a coarse resolution, thanks to the high sensitivity of neutron imaging to hydrogen additional spatial information on the water absorption process has been gathered. In particular, the depth of water penetration and the heterogeneous distribution of water inside the pore network could affect the depth and intensity of the degradation process during subsequent drying and water absorption cycles.

Acknowledgments The authors are very grateful to José Teixeira for his kind and valuable support during the experimental session performed at LLB, CEA/Saclay in May 2015 and for his precious suggestions that greatly improved the quality of the present research.

References

1. UNI EN 10859, in *Natural Stone Test Methods—Determination of Water Absorption by Capillarity*, ed. by UNI (Milano, Italy, 2000)
2. M. Steiger, A.E. Charola, in *Stone in Architecture*, ed. by S. Siegesmund, R. Snethlage (Springer, Berlin Heidelberg, 2011)
3. D. Capitani, V. Di Tullio, N. Proietti, *Prog. Nucl. Magn. Reson. Spectrosc.* **64**, 29 (2012)
4. N. Proietti, D. Capitani, V. Di Tullio, *Sensors* **14**, 6977 (2014)
5. V. Cnudde, M. Boone, *Earth-Sci. Rev.* **123**, 1 (2013)
6. E. Perfect, C.L. Cheng, M. Kanga, M.Z. Bilheux, J.M. Lamanna, M.J. Gragg, D.M. Wright, *Earth-Sci. Rev.* **129**, 120 (2014)
7. H. Pleinert, C. Degueldre, *J. Contam. Hydrol.* **19**, 29 (1995)
8. F.C. de Beer, M.F. Middleton, *S. Afr. J. Geol.* **109**, 541 (2006)
9. J.K. Jasti, H.S. Fogler, *AIChE J.* **38**, 481 (1992)
10. R. Hassanein, H.O. Meyer, A. Carminati, M. Estermann, E. Lehmann, P. Vontobel, *J. Phys. D Appl. Phys.* **39**, 4284 (2006)
11. V. Cnudde, M. Dierick, J. Vlassenbroeck, B. Masschaele, E. Lehmann, P. Jacob, L. van Hoorebeke, *Nucl. Instrum. Methods Phys. Res. B* **266**, 155 (2008)
12. J. Prazak, J. Tywoniak, F. Peterka, T. Slonc, *Int. J. Heat Mass Transf.* **33**, 1105 (1990)
13. H. Pleinert, H. Sadouki, F.H. Wittmann, *Mater. Struct.* **31**, 218 (1998)
14. J. Dewanckele, T. De Kock, G. Fronteau, H. Derluyn, P. Vontobel, M. Dierick, L. van Hoorebeke, P. Jacobs, V. Cnudde, *Mater. Charact.* **88**, 86 (2014)
15. B. Masschaele, M. Dierick, L. van Hoorebeke, V. Cnudde, P. Jacobs, *Environ. Geol.* **46**, 486 (2004)
16. M. Dierick, J. Vlassenbroeck, B. Masschaele, V. Cnudde, L. van Hoorebeke, A. Hillenbach, *Nucl. Instrum. Methods Phys. Res. A* **542**, 296 (2005)
17. T. Nemeč, J. Rant, V. Apih, B. Glumac, *Nucl. Instrum. Methods Phys. Res. A* **24**, 242 (1999)
18. M. Zawisky, F. Hameed, E. Dyrnjaja, J. Springer, A. Rohatsch, *Nucl. Instrum. Methods Phys. Res. B* **268**, 2446 (2010)
19. P. Van den Heede, B. Van Belleghem, N. Alderete, K. Van Tittelboom, N. De Belie, *Materials* **9**, 311 (2016)
20. A. Bellanca, E. Curcuruto, S. Lo Bue, R. Neri, *Miner. Petrogr. Acta* **42**, 193 (1999)
21. R.L. Folk, *Am. Assoc. Pet. Geol. Bull.* **43**, 38 (1959)
22. R.J. Dunham, in *Classification of Carbonate Rocks*, ed. by E. Ham (American Association of Petroleum, Tulsa, 1962), p. 21
23. P.W. Choquette, L.C. Pray, *Am. Assoc. Pet. Geol. Bull.* **54**, 250 (1970)
24. G. Barone, P. Mazzoleni, G. Pappalardo, S. Raneri, *Constr. Build. Mater.* **95**, 355 (2015)
25. UNI EN 12370, in *Natural Stone Test Methods—Determination of Resistance to Salt Crystallization*, ed. by UNI (Milano, Italy, 2001)
26. M.D. Abramoff, J. Magalhães Paulo, J. Ram Sunanda, *Biophotonics Int.* **11**, 36 (2004)
27. F.H. Kim, D. Penumadu, D.S. Hussey, *J. Geotech. Geoenviron. Eng.* **138**, 147 (2012)
28. J.R. Philip, *Soil Sci.* **83**, 345 (1957)
29. G. Cultrone, M.J. de la Torre, E. Sebastián, O. Cazalla, *Mater. de Constr.* **53**, 41 (2003)
30. C. Hammecker, D. Jeannette, *Transp. Porous Media* **17**, 285 (1994)
31. S. Raneri, V. Cnudde, T. De Kock, H. Derluyn, G. Barone, P. Mazzoleni, *Eur. J. Miner.* **27**, 279 (2015)